The effect of carbon supports on the electrocatalytic performance of Ni-N-C catalysts for CO2 reduction to CO

Fu, Shilong; Izelaar, Boaz; Li, Ming; An, Qi; Li, Min; de Jong, Wiebren; Kortlever, Ruud

DOI
10.1016/j.nanoen.2024.110461

Publication date
2025

Document Version
Final published version

Published in
Nano Energy

Nano Energy 133 (2025) 110461

Contents lists available at ScienceDirect

Nano Energy

journal homepage: www.elsevier.com/locate/nanoen

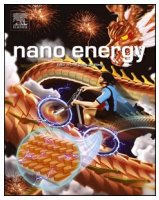

Full paper

The effect of carbon supports on the electrocatalytic performance of Ni-N-C catalysts for CO_2 reduction to CO

Shilong Fu [a], Boaz Izelaar [a], Ming Li [a,b], Qi An [c], Min Li [a,d], Wiebren de Jong [a], Ruud Kortlever [a,*]

[a] Section of Large-scale Energy Storage, Department of Process and Energy, Faculty of Mechanical, Maritime and Materials Engineering, Delft University of Technology, Leeghwaterstraat 39, Delft, CB 2628, the Netherlands
[b] Section of Product and Process Engineering, Department of Chemical Engineering, Faculty of Applied Sciences, Delft University of Technology, Van der Maasweg 9, Delft, HZ 2628, the Netherlands
[c] Section of Complex Fluid Processing, Department of Process and Energy, Faculty of Mechanical, Maritime and Materials Engineering, Delft University of Technology, Leeghwaterstraat 39, Delft, CB 2628, the Netherlands
[d] Section of Catalysis Engineering, Department of Chemical Engineering, Faculty of Applied Sciences, Delft University of TechnologyVan der Maasweg 9, Delft, HZ 2628, the Netherlands

ARTICLE INFO

Keywords:
Electrochemical CO_2 reduction
Electrocatalysis
Carbon-based catalysts
Nickel-nitrogen-carbon catalysts
Structure-performance correlations

ABSTRACT

Carbon-supported nickel and nitrogen co-doped (Ni-N-C) catalysts have been extensively studied as selective and active catalysts for CO_2 electroreduction to CO. Most studies have focused on adjusting the coordination structure of Ni-N_x active sites, while the impact of the carbon supports has often been overlooked. In this study, a series of Ni-N-C catalysts on different carbon supports, including carbon black (CB), multi-walled carbon nanotubes (CNT), and activated nitrogen-doped biochar (ANBC), were synthesized using a ligand-mediated method. The effect of the carbon support on the electrocatalytic performance for CO_2 reduction was investigated at both low current densities, in a H-cell, and high current densities, in a MEA electrolyzer. All of the prepared Ni-N-C catalysts show good faradaic efficiencies (FE) toward CO production (up to ~90 %), however, the onset potentials and partial current densities for CO production vary greatly. The textural properties of the carbon support and the distribution of Ni-N_x active sites on the carbon support are demonstrated as the main factors behind the performance differences. In particular, hierarchical porous structures with a large specific surface area are helpful to facilitate mass transport and improve the dispersion of active sites, which allows for a better CO_2 reduction performance of Ni-N-ANBC compared to Ni-N-CB and Ni-N-CNT. This study demonstrates the importance of the carbon support for Ni-N-C catalysts and provides new insights into the design of efficient Ni-N-C catalysts for the CO_2RR.

1. Introduction

With the growing global climate problems caused by excessive CO_2 emissions, the need for accelerating the deployment of carbon neutral energy and production technologies has become stronger [1,2]. The electrochemical CO_2 reduction reaction (CO_2RR) powered by renewable electricity is a promising technology to convert waste CO_2 into chemicals and fuels. Thereby, the process can store surplus electricity from intermittent sources, such as wind and solar, into chemical bonds [3–7]. Depending on the choice of catalysts, CO_2 can be reduced to CO [8], formate [9], CH_4 [10], C_2H_4 [11] and oxygenated hydrocarbons. Among these products, CO is considered as an attractive and competitive product [12]. The two electron reduction of CO_2 to CO exhibits a relatively high product selectivity with a relatively low energy cost [13]. In addition, CO can be widely used in downstream chemical transformations, such as Fischer-Tropsch synthesis [14]. However, due to the inevitable competition with the hydrogen evolution reaction (HER), the CO_2RR in aqueous electrolytes still faces many challenges [15]. Therefore, seeking active, efficient, stable and cost-effective catalysts remains an important challenge for the application of CO_2RR technology. Recently, transition metal and nitrogen co-doped carbon materials, hereinafter referred to as M-N-C, were demonstrated as efficient catalysts for the CO_2RR [16]. The M-N_x structures (a central metal coordinatively bound to different amounts of N atoms) are identified as the active sites for the CO_2RR [17]. Many studies have reported that varying the central metal, such as Fe, Co, and Ni, resulted in a different product

* Corresponding author.
E-mail address: r.kortlever@tudelft.nl (R. Kortlever).

https://doi.org/10.1016/j.nanoen.2024.110461
Received 9 June 2024; Received in revised form 7 August 2024; Accepted 7 November 2024
Available online 8 November 2024

selectivity and activity for the CO_2RR [18–21]. In particular, the coordinative Ni-N_x sites show favorable energetics for CO_2 activation and reduction which results in a high CO faradaic efficiency. Möller et al. reported a Ni-N-C catalyst integrated in a gas diffusion electrode (GDE) electrolyzer and showed a stable performance with 85 % faradaic efficiency and 200 mA/cm^2 partial current density toward CO over a 20 hours test, at an applied potential of −1.1 V vs. RHE [22]. Zheng et al. used a Ni-N-C catalyst in a 10 × 10 cm membrane electrode assembly (MEA) system, which showed an average current of ~8 A and over 90 % faradaic efficiency toward CO during 6 hours electrolysis at a cell voltage of 2.8 V [23]. In comparison to Ag and Au electrocatalysts, inexpensive Ni-N-C catalysts display competitive performances and show great potential for large-scale application.

To further improve the catalytic performance and reveal the active sites and reaction mechanisms of Ni-N-C catalysts, many studies have adjusted the coordination structures of Ni-N_x sites [24,25]. Surprisingly, Ni-N_4, Ni-N_3 (Ni coordinate with three nitrogen atoms), and Ni-VN_3 (V is a coordination vacancy of Ni centers) have all been demonstrated as the most active sites, experimentally and theoretically [26–28]. This shows the complexity of the exact reaction mechanism of these materials. On the other hand, altering the morphology and pore structure of carbon materials is also considered to be an effective strategy to improve the performance of Ni-N-C catalysts for CO_2RR. For instance, the Strasser group pointed out that "the reaction rate is not determined by the kinetics of the CO_2RR on the active site but rather to the CO_2 transport to those sites" [29]. Therefore, it is crucial to improve the accessibility of active sites by tuning the physicochemical properties (porosity, hydrophobicity, etc.) of carbon supports to enhance the catalytic performance of Ni-N-C catalysts. In the past few years, carbon black [23], carbon nanotubes [30], graphene [31], and other carbon supports which were made from carbonization of different carbon precursors [32–36], were widely used to synthesize Ni-N-C catalysts for the CO_2RR and most of them show excellent performances. However, most of the existing studies mainly focus on the importance of the Ni-N_x sites, overlooking the contribution of the carbon supports. Therefore, the role of different carbon supports and the interaction between the carbon support and Ni-N_x sites remains poorly understood. In addition, due to the diversity of catalyst preparation methods, reactor types and sizes, and reaction parameters, it is hard to deduce how these different carbon supports affect the catalytic performance for the CO_2RR by simply comparing the results from previous publications [37]. Overall, it is crucial to understand the influence of the carbon support properties on the performance of Ni-N-C catalysts, as it will help to further optimize the performance of Ni-N-C catalysts.

In order to study the influence of carbon supports on the CO_2-reduction performance of Ni-N-C, we synthesized a series of Ni-N-C catalysts via a ligand mediated method, with commercial carbon black (CB), multi-walled carbon nanotube (CNT), and a self-made activated N-doped biochar (ANBC) as different carbon supports. The effects of the different carbon supports on the electrochemical performance are studied on a fundamental level in an H-cell, and under more industrially relevant conditions in a MEA cell. Additionally, the physicochemical properties of different carbon supports, such as hydrophobicity, surface roughness, porosity, the abundance of defects, and the distribution of active sites are comprehensively analyzed. All prepared Ni-N-C catalysts show roughly 90 % FE_{CO}, but also exhibit significant differences in current densities and onset potentials. The textural properties of the carbon support and the distribution of Ni-N_x active sites mutually influence the performance of Ni-N-C catalysts for CO_2RR. In particular, carbon supports with hierarchical porous structures help to enhance mass transfer, large specific surface area improves the dispersion of Ni-N_x active sites. These factors make Ni-N-ANBC exhibit a better CO_2RR performance than other samples. These results emphasize the importance of carbon support for the CO_2RR performance of Ni-N-C catalyst and provide guideline for the optimization of carbon supports.

2. Experimental section

All chemicals were used as received without further purification. Aqueous solutions were prepared from ultrapure water (Milli-Q IQ 7000, 18.2 MΩ).

2.1. Catalyst preparation

2.1.1. Synthesis of ANBC

The activated N-doped biochar (ANBC) was prepared according to a procedure outlined in our previous study [38]. In brief, the ANBC was synthesized by a one-step pyrolysis method, where 5 g of sugarcane bagasse powder, 10 g of urea and 15 g of NaOH (mass ratio: 1:2:3) were added into a crucible and mixed homogeneously. The mixture was transferred to a furnace, heated at 800 °C for 1 h with a ramping rate of 10 °C/min under a N_2 atmosphere (100 sccm, 99.99 %, Linde gas). Afterwards the furnace was cooled to room temperature. The black powder collected after pyrolysis was dispersed in 1 M HCl for 4 h at 60 °C to remove the residual sodium containing salts and other impurities. After the acid wash, the black powder was filtered and rinsed with ultrapure water until it reached a neutral pH. Finally, the activated N-doped biochar was dried in an oven (105 °C) for 12 h. The end product was denoted as ANBC.

2.1.2. Synthesis of Ni-N-C catalysts

The Ni-N-C catalysts were synthesized according to a ligand-mediated method reported by Yang et al. with slight modifications [39]. 8.3 mg nickel(II) acetate tetrahydrate (Sigma-Aldrich, 99.995 %) and 23.2 mg 1,10-phenanthroline monohydrate (Sigma-Aldrich, 99 %) were dispersed in 50 mL of methanol (VWR Chemical, 99.8 %) and stirred for 20 min at room temperature. The molar ratio of Ni to the ligand was 1: 3.5. An excess of 1,10-phenanthroline was used to guarantee a high dispersion of the metal centers to form Ni-N_x sites instead of Ni nanoparticles on the carbon supports. Subsequently, either 100 mg carbon black (Vulcan XC 72 R), multi-wall carbon nanotubes (Sigma-Aldrich) or ANBC was added into the solution. The molar ratio of Ni to carbon is approximately 1: 250, and the calculated weight percentage of Ni is approximately 1.5 wt%. Then, the solution was heated at 60 °C for 4 h under continuous stirring. Afterward, the solution was transferred to a vacuum oven and heated at 60 °C for 12 h to evaporate the solvent. The obtained black solid was ground in a mortar and then transferred into an alumina crucible and placed in a tubular furnace. The furnace was first purged with argon at a flow rate of 500 sccm for 1 h to remove all residual air, then heated to 600 °C with a ramping rate of 5 °C/min under an argon atmosphere (250 sccm, 99.99 %, Linde gas) and held at 600 °C for 2 h. After cooling down to room temperature naturally, the black powder was collected and ground one more time. The final products were designated as Ni-N-CB, Ni-N-CNT, and Ni-N-ANBC, respectively.

2.1.3. Synthesis of Ni-C catalysts

For comparison, Ni-C catalysts were prepared using the same procedure as Ni-N-C catalysts but without adding 1,10-phenanthroline monohydrate. The obtained products were recorded as Ni-CB, Ni-CNT, and Ni-ANBC, respectively.

2.2. Characterization

Scanning electron microscopy (SEM) images were taken on a JEOL JSM-6500F microscope with an acceleration voltage of 15 kV. Transmission electron microscopy (TEM) images were obtained using a JEOL JEM1400 microscope, operating at an acceleration voltage of 120 kV. For high-resolution transmission electron microscopy (HRTEM) analysis, a FEI cubed Cs-corrected Titan electron microscope was used. HRTEM lattice images were collected using a Thermo Scientific Ceta 16 M camera. In scanning transmission electron microscopy (STEM)

mode, annular dark field (ADF) images were collected. In this mode, a subnanometer beam is scanned over the electron-transparent sample, and diffracted electrons are collected on a ring-shaped detector for each beam position. Elemental mapping in STEM mode was performed using the super-X detector in the ChemiSTEM configuration, with energy-dispersive X-ray (EDX) spectra collected for each beam position in a STEM image. The accelerating voltage for both STEM and TEM was 300 kV. Powder X-ray diffraction (XRD) patterns were measured with a Bruker AXS D2 Phaser diffractometer with Cu Kα radiation (λ = 0.15406 nm), the scanning 2θ range was between 10° to 90° using a step length of 0.02°. X-ray photoelectron spectroscopy (XPS) measurements were carried out on a Thermo Scientific K-Alpha system using a monochromatic Al Kα X-ray source (1486.6 eV). CasaXPS (Version 2.3.22PR1.0) software was used for the elemental oxidation state identification and peak deconvolution of the XPS spectra. Contact angle measurements were performed using a standard goniometer setup (OCA25, DataPhysics Instruments, Germany) implementing the sessile drop method. For the static contact angle measurements, a 2 μL droplet was dispensed onto the substrate using an automatic pipetting unit. The contact angle was photographed and measured by the goniometer software (SCA 20). For the dynamic contact angle measurements, a liquid-dispensing syringe was placed 5 mm above the substrate and a 10 μL droplet was gently dispensed. Then the volume of the droplet was first increased from 10 μL to 30 μL and then decreased to 10 μL at a rate of 0.16 μL/s, which was controlled by an electronic dosing system. The increase-decrease procedure was carried out 2 times and the contact angle and the diameter of the drop base were recorded every second by the SCA 20 software. All measurements were taken in ambient air and the temperature remained between 21 and 24 °C. N_2 adsorption-desorption isotherms were recorded at 77 K using a Micromeritics TriStar II 3020 instrument. Samples were degassed at 300 °C for 15 h before measurement. Specific surface areas were determined by the Brunauer-Emmett-Teller (BET) method and pore size distribution were calculated using a Density Functional Theory (DFT) model. Raman spectra were recorded from 500 to 3000 cm^{-1} on a Horiba Scientific LabRAM HR Evolution Raman Spectroscopy system with an excitation wavelength of 514 nm. The content of Ni in the catalysts was measured by inductively coupled plasma optical emission spectroscopy (ICP-OES, Spectro Arcos).

2.3. Electrodes preparation

Working electrodes for H-cell measurements were prepared by drop casting via the following method. First, 4 mg of catalyst was dispersed into a solvent mixture containing 950 μL isopropanol and 50 μL of 5 % Nafion perfluorinated resin solution (Sigma-Aldrich). The mixture was sonicated for 1 h to obtain a homogeneous ink. Afterwards, 10 μL of the catalyst ink was drop casted on a 1 cm^2 cut disc of carbon paper (Toray carbon paper, TGP-H-60, Thermo scientific) and dried at room temperature to obtain a catalyst loading of approximately 0.04 mg/cm^2. A 25 mm × 25 mm × 1 mm platinum foil (99.9 %, Mateck) was used as the counter electrode, which was cleaned by flame annealing at least 3 times to remove any possible impurities before use. A leak-free Ag/AgCl electrode (40 mm length, Innovative instrument, USA) was used as reference electrode. The potential drift of the reference electrode was checked before each experiment by comparing it with a master Ag/AgCl reference electrode (BASi, MF-2056, USA), which is always kept in pristine working condition. Deviations between the tested and master reference electrode were always below 5 mV.

Cathode and anode for MEA cell measurements were prepared by spray coating. The cathode catalyst ink was prepared following the same recipe as aforementioned. The dispersed ink was spray-coated on a 2.25 cm × 2.25 cm carbon gas diffusion layer (GDL, Sigracet 39 BB, Fuel Cell Store), using a hand-held airbrush (Conrad HP-101) with 0.3 mm nozzle and nitrogen as carrier gas. The GDL substrates were fixed on a hot plate at 100 °C to improve drying. To prepare the anode, 1 mL catalyst ink was prepared containing 20 mg iridium oxide nanoparticles (Alfa Aesar, 99.99 %), 475 μL isopropanol, 475 μL water and 50 μL 5 % Nafion ionomer, and the ink was sonicated 20 min before use. [40] The dispersion was spray-coated on a 3 cm × 3 cm × 0.045 cm titanium GDL (Bekaert). As received titanium GDLs were ultrasonicated in acetone, ethanol and water to remove any possible impurities before use. The GDEs were weighed before and after spray coating to quantify the loading. The cathode catalyst loading was 0.5 ± 0.05 mg/cm^2 and the anode catalyst loading 1.0 ± 0.1 mg/cm^2.

2.4. Electrochemical measurements

Working electrodes were tested in a compact H-cell inspired by Lobaccaro et al. [41]. Each compartment contained 1.8 mL of 0.1 M $KHCO_3$ as electrolyte and the cathode and anode chambers were separated by an anion-exchange membrane (Selemion AMV, AGC Engineering). Before each experiment, the catholyte was purged with CO_2 for 15 min to obtain a CO_2-saturated 0.1 M $KHCO_3$ electrolyte with pH = 6.8. Electrochemical measurements were carried out using a Biologic SP-200 potentiostat (Biologic, France). A schematic illustration of the setup is shown in Figure S1. All measured potentials were converted to the reversible hydrogen electrode (RHE) scale according to the formula: E (V vs. RHE) = E (V vs. Ag/AgCl) + 0.197 + 0.059 × pH. Linear sweep voltammetry (LSV) measurements were recorded in CO_2-saturated (pH = 6.8) and Ar-saturated (pH = 8.3) 0.1 M $KHCO_3$ electrolytes at a scan rate of 5 mV/s. The electrochemically active surface areas (ECSA) of the electrodes were determined by measuring the double layer capacitance (C_{dl}), which was derived from cyclic voltammetry measurements with a scan rate of 5, 10, 25, and 50 mV/s in a potential window between 0.45 and 0.55 V vs. RHE. The C_{dl} was estimated by plotting the Δj ($j_a - j_c$)/2 at 0.50 V vs. RHE against the scan rates, where the slope of the plot represents the C_{dl}. Chronoamperometric electrolysis measurements (with iR compensation) were carried out at different applied potentials from −0.50 to −1.15 V vs. RHE and each potential was applied for 1 h. The cell resistance (R_s) was measured by applying a potentiostatic electrochemical impedance spectrometry (PEIS) test from 200 kHz to 100 mHz. The potentiostat can only compensate 85 % of R_s automatically during the CO_2RR measurements, thus the remaining 15 % was corrected manually afterwards. During the chronoamperometry tests, CO_2 was purged continuously into the catholyte with a flow rate of 8 sccm using a mass flow controller. The FEs reported in this study for gas products were determined using the data collected from 42 min to 54 min, which show a relatively stable current and gas product composition.

All prepared gas diffusion electrodes were tested in a 5 cm^2 flow field MEA cell (Dioxide materials) with a serpentine flow channel on the cathode and anode endplate. The MEA cell was assembled by sandwiching a 5 cm × 5 cm anion exchange membrane (PiperION, 20 microns, Fuel Cell Store) between the prepared cathode electrode and anode electrode, using eight bolt screws (2 Nm was applied). The humidified CO_2 was supplied to the cathode compartment at a flow rate of 20 sccm, and the anode compartment was circulated with 1 M $KHCO_3$ at 5 mL/min using a peristaltic pump. A mass flow meter (Bronkhorst) was used to record the flow rate at the outlet of the reactor (Figure S2). A series of CO_2RR measurements were performed with a stage-increasing constant current method, ranging from 25 to 250 mA/cm^2, where each current was applied for 25 min. The faradaic efficiency was determined by collecting the average values of the last 10 min for each current, where a relatively stable gas product composition was measured.

2.5. Product quantification

The gaseous CO_2 reduction products were analyzed by an inline gas chromatograph every 2 min, using a CompactGC 4.0 (Global analyser solutions, The Netherlands) equipped with one flame ionization detector (FID) to analyze hydrocarbon compounds and two thermal conductivity detectors (TCD) to analyze CO and H_2, respectively. The GC was

calibrated using calibration gas cylinders (Linde Gas Benelux B.V.) with five different concentrations of analytes (50, 100, 1000, 3000, and 8000 ppm of H_2, CO, CH_4 and C_2H_4) in CO_2. An aliquot of the catholyte was collected at the end of the H-cell CO_2RR measurements and the liquid products were quantified using a high-performance liquid chromatograph (HPLC, Agilent 1260 Infinity), equipped with two Aminex HPX 87-H columns (Bio-Rad) placed in series. The column oven was maintained constant at 60 °C, using a 1 mM H_2SO_4 aqueous solution as eluent with a steady flow of 0.6 mL/min and applying a refractive index detector (RID) for product detection.

3. Results and discussions

3.1. Catalyst characterization

The morphologies and microstructures of Ni-N-C catalysts were visualized using scanning electron microscopy (SEM) and transmission electron microscopy (TEM). SEM images of the Ni-N-C catalysts (Fig. 1a, b and c) show interconnected nanoporous structures with multilevel channels. The TEM image of Ni-N-CB (Fig. 1d) exhibits the representative nanosphere-stacked morphology of carbon black, whereas Ni-N-CNT (Fig. 1e) shows a structure of cross-linked multi-walled carbon nanotubes, and Ni-N-ANBC (Fig. 1f) shows a crumpled nanosheet-like morphology. The HRTEM and HAADF-STEM-EDS images reveal the absence of nickel nanoparticles and indicate the uniform dispersion of Ni-N_x active sites over the catalysts (Figure S3). As comparison, a multitude of Ni nanoparticles can be observed over the Ni-C catalysts (see Figure S4), indicating that 1,10-phenanthroline isolates the Ni species effectively and prevents Ni nanoparicles formation. The TEM image of pristine ANBC (Figure S4g) shows that no additional particulate contaminations exist on the self-made activated N-doped biochar.

Fig. 2a shows the X-ray diffraction (XRD) patterns of the prepared Ni-N-C catalysts. The two broad diffraction peaks located at around $2\theta = 25^\circ$ and 44° correspond to the (002), and (100) planes of graphitic carbon, respectively. Although the (200) crystal plane of NiO may overlap with the (100) plane of carbon at around $2\theta = 44^\circ$, no other obvious diffraction peaks of NiO can be observed. In contrast, the XRD patterns of Ni-C materials (Figure S5) show two additional diffraction peaks at around $2\theta = 37^\circ$ and 63°, which can be readily indexed as the (111) and (220) crystal planes of NiO [42]. The more distinct NiO peaks in the Ni-C catalysts are likely attributed to the higher Ni content in these materials compared to the Ni-N-C materials. The theoretical Ni weight percentage in the Ni-C catalysts is 1.92 wt%, which is higher than the 1.49 wt% in the Ni-N-C catalysts due to the absence of the ligand (1,10-phenanthroline monohydrate). The ICP results show the Ni weight percentages in Ni-CB, Ni-CNT, and Ni-ANBC to be 1.70 %, 1.65 %, and 1.71 %, respectively, which are higher than the corresponding values in Ni-N-CB, Ni-N-CNT, and Ni-N-ANBC at 1.11 %, 1.14 %, and 1.09 %, respectively. In addition, the XRD patterns of the pristine carbon materials (Figure S5) only display the feature peaks of graphitic carbon.

The chemical composition of Ni-N-C catalysts was investigated by X-ray photoelectron spectroscopy (XPS). The survey spectra (Fig. 2b) reveal the presence of C, N, O and Ni. The high-resolution N 1 s spectra (Fig. 2c) can be deconvoluted into pyridinic N (~398.2 eV), Ni-N (~399.2 eV), pyrrolic N (~400.2 eV), graphitic N (~401.8 eV), and oxidized N (~404.7 eV) [28,43]. The Ni-N-CB and Ni-N-CNT samples are dominated by a Ni-N signal, which is in line with the results from Xi et al. [44]. Since Ni-N-ANBC used N-doped biochar as a support, it shows a more complex N 1 s spectrum which contains all N-containing species. The high-resolution Ni 2p spectra (Fig. 2d) of Ni-N-C catalysts show that the binding energy of Ni $2p_{3/2}$ is concentrated around 855.1 eV, indicating that the valence state of the Ni-N_x species in all Ni-N-C catalysts is the same. The binding energy of Ni $2p_{3/2}$ is higher than that of Ni^0 in Ni metal (852.6 eV), suggesting the absence of metallic Ni [45–47]. The XPS spectra and chemical compositions of pristine carbon and Ni-C materials are summarized in Figure S6 and Table S1. The high-resolution N 1 s spectra of CB and CNT indicate that no additional nitrogen was induced into the pristine carbon materials. Similarly, the high-resolution Ni 2p spectra of CB, CNT, and ANBC indicates that no Ni-containing impurities existed in the pristine carbon supports. Remarkably, Ni-ANBC also features peaks of a Ni-N structure in the high-resolution N 1 s spectrum (Figure S6h), which can be attributed to partial coordination of N-containing defects on the surface of ANBC with free Ni^{2+} to form a stable Ni-N_x structure [48].

In summary, we have successfully synthesized a series of Ni-N-C

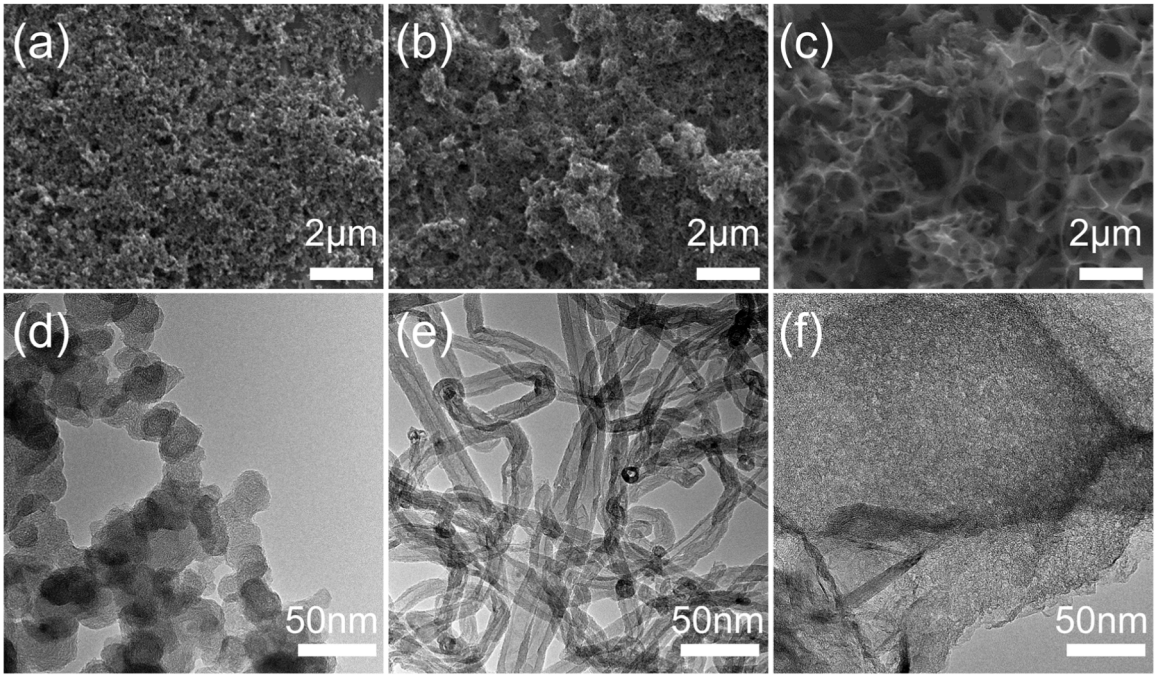

Fig. 1. SEM images of (a) Ni-N-CB, (b) Ni-N-CNT, (c) Ni-N-ANBC, and TEM images of (d) Ni-N-CB, (e) Ni-N-CNT, (f) Ni-N-ANBC.

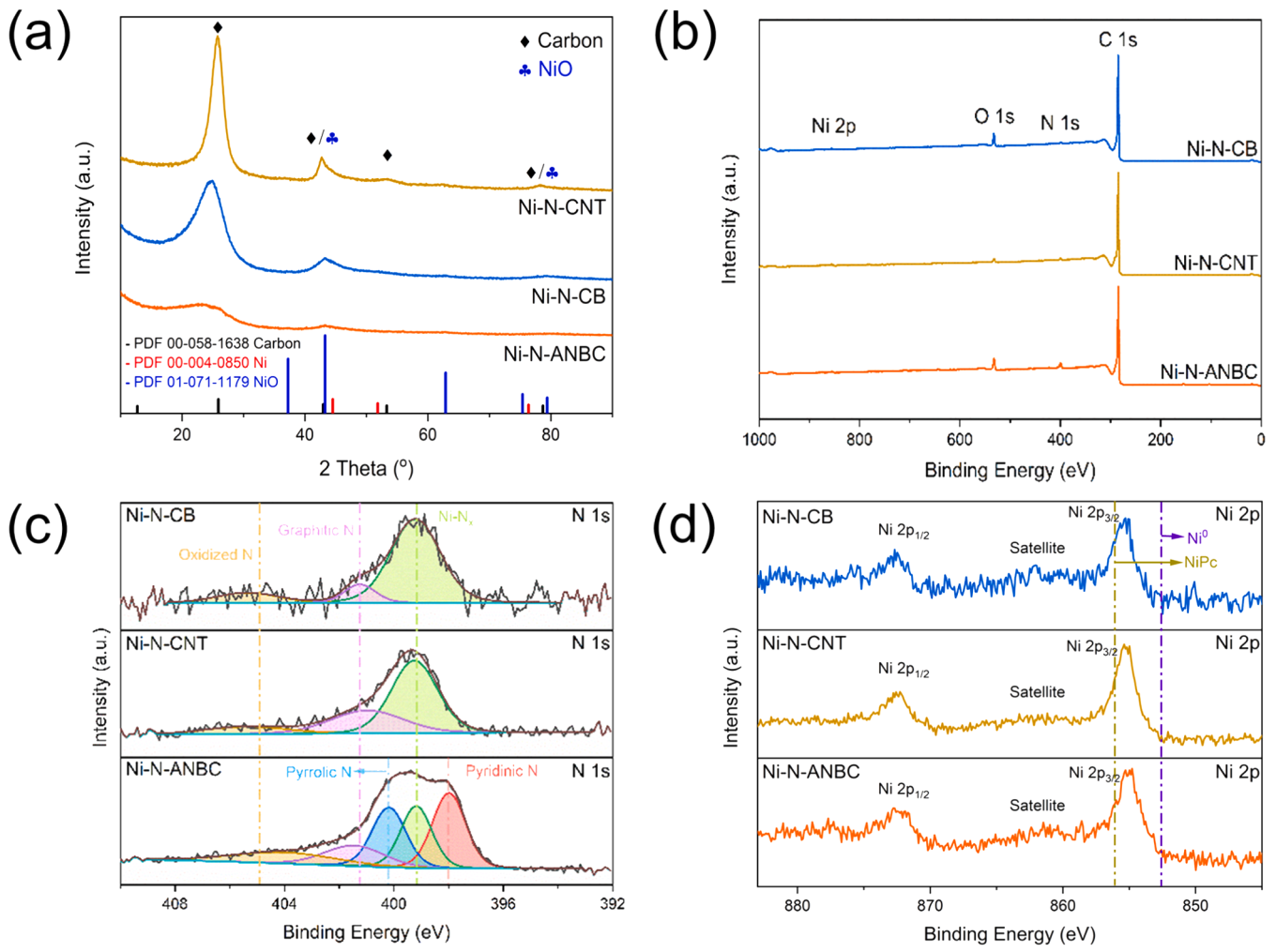

Fig. 2. (a) XRD patterns, (b) XPS full survey, (c) High-resolution N 1 s XPS spectra, (d) High-resolution Ni 2p XPS spectra of Ni-N-CB, Ni-N-CNT, and Ni-N-ANBC.

catalysts on different carbon supports via a ligand-mediated method. No obvious Ni-containing nanoparticles can be observed in Ni-N-C catalysts by TEM and XRD. Combining the analysis of XPS high-resolution N 1 s and Ni 2p spectra, we confirm the prevalent presence of Ni-N_x moieties in all Ni-N-C catalysts. In addition, XRD and XPS characterization confirms that no apparent impurities originate from the pristine carbon supports. Therefore, any distinction in electrochemical performance for CO_2RR can be ascribed to carbon support-related factors.

3.2. *Electrocatalytic performances*

The electrocatalytic performance of the Ni-N-C catalysts toward the CO_2RR were first evaluated in a compact H-cell. Linear sweep voltammograms of the Ni-N-C catalysts in Ar-saturated and CO_2-saturated 0.1 M $KHCO_3$ electrolytes are shown in Figure S7. All of the Ni-N-C catalysts exhibit a higher current density in a CO_2-saturated electrolyte than in an Ar-saturated electrolyte, suggesting that the catalysts possess activity for the CO_2RR. The voltammograms of Ni-N-C catalysts in a CO_2-saturated electrolyte are depicted in Fig. 3a, and show that the CO_2 reduction onset potential of Ni-N-CNT is lower than that of Ni-N-CB and Ni-N-ANBC. As a comparison (Figure S7), Ni-CB and Ni-CNT have no activity for the CO_2RR whereas ANBC and Ni-ANBC both show activity for the CO_2RR, which is attributed to contributions from the N-doped biochar [38,49].

To further evaluate the catalytic performance of the Ni-N-C catalysts, chronoamperometry measurements were performed in a potential window from −0.5 V to −1.15 V vs. RHE (with iR compensation). CO and H_2 are detected as dominant gaseous products while no liquid products were detected in the catholyte. The FE toward CO for the different Ni-N-C catalysts are presented in Fig. 3b. All of the Ni-N-C catalysts show a good FE_{CO} (up to ~90 %) in different potential windows. In particular, the FE_{CO} of Ni-N-CB increases from −0.5 V to −0.8 V vs. RHE, reaches a maximum of 88 % FE_{CO} at −0.8 V vs. RHE and then decreases from −0.8 V to −1.11 V vs. RHE. Ni-N-CNT shows a higher FE_{CO} than other samples from −0.5 V to −0.8 V vs. RHE. It maintains ~90 % FE_{CO} from −0.6 V to −1.03 V vs. RHE, with a decrease to 66 % at −1.13 V vs. RHE. The FE_{CO} of Ni-N-ANBC exhibits an increasing trend from −0.5 V to −0.83 V vs. RHE and then reaches a high FE_{CO} (>90 %, maximum 97 % at −0.93 V vs. RHE) from −0.82 V to −1.15 V vs. RHE. With respect to the total current density (j_{Total}) (Fig. 3c) and partial current density of CO (j_{CO}) (Fig. 3d), Ni-N-CB shows a lower catalytic activity than the other samples over the entire potential window. Ni-N-CNT and Ni-N-ANBC exhibit a comparable catalytic activity, where Ni-N-CNT shows a higher j_{CO} from −0.5 V to −0.83 V vs. RHE and Ni-N-ANBC shows a higher j_{CO} from −0.83 V to −1.15 V vs. RHE. The turnover frequencies (TOFs) of Ni-N-C catalysts are depicted in Figure S8. Ni-N-ANBC achieves a maximum TOF of 9185 h^{-1} at −1.13 V vs. RHE. Ni-N-CB and Ni-N-CNT reach maximum TOF values of 1857h^{-1} and 6790 h^{-1}, respectively, at around −1.0 V vs. RHE. The FEs toward H_2 (FE_{H2}) and partial current densities toward H_2 (j_{H2}) of Ni-N-C catalysts are presented in Figure S9, with the FE_{H2} showing an opposite trend to that of FE_{CO} and Ni-N-ANBC showing the lowest j_{H2} values, indicating that it is least active for the hydrogen evolution reaction (HER). Additionally, Figure S10 summarizes the electrochemical

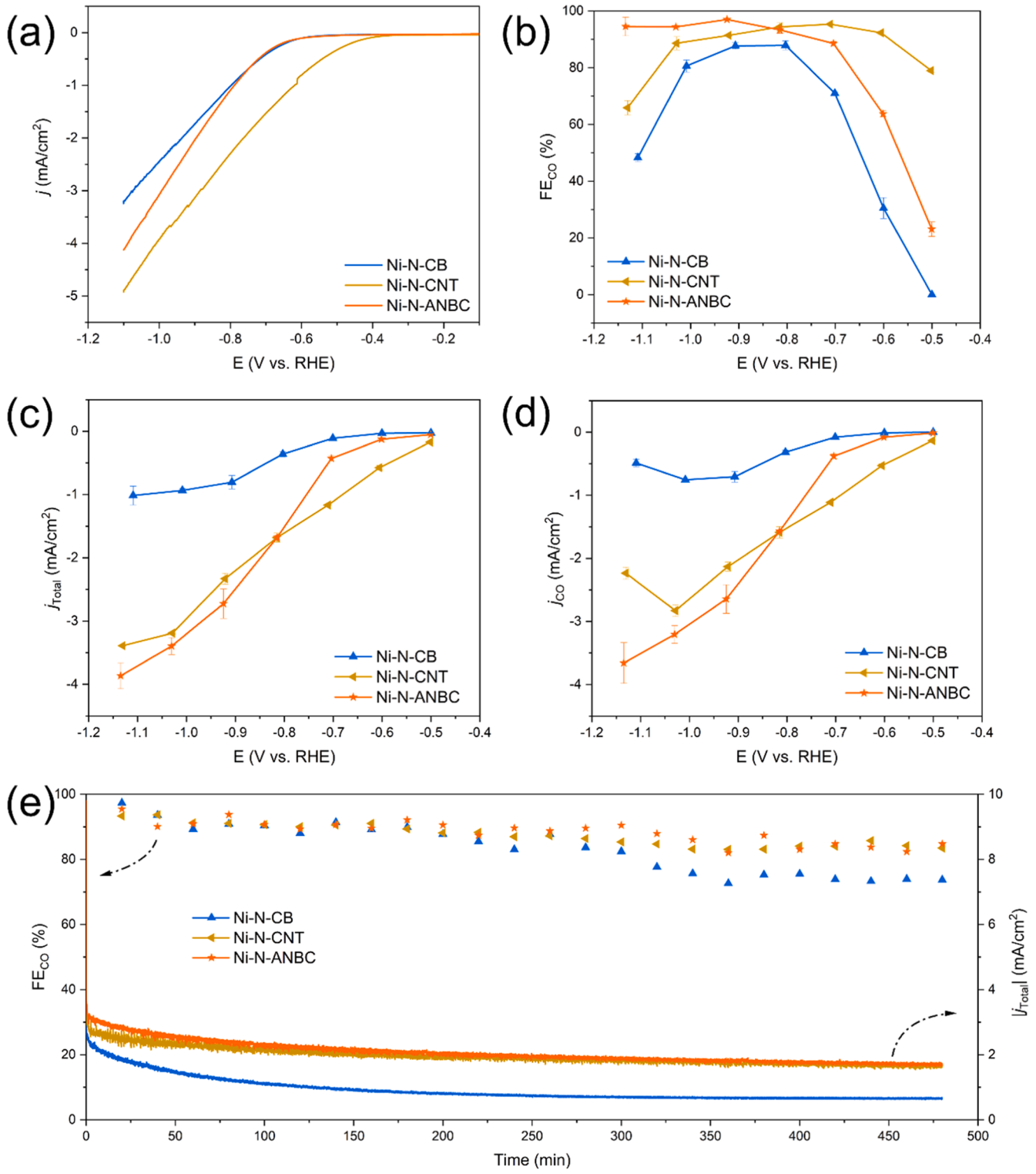

Fig. 3. (a) Linear sweep voltammograms in a CO_2-saturated 0.1 M $KHCO_3$ electrolyte, (b) Faradaic efficiency toward CO, (c) Total current density and (d) Partial current density toward CO during CO_2 electrolysis in the same electrolyte at different potentials and (e) 8 h stability tests at −0.9 V vs. RHE of Ni-N-CB, Ni-N-CNT, and Ni-N-ANBC.

performances for the CO_2RR of all prepared samples (Ni-N-C, Ni-C, and ANBC). It is clear that both Ni-CB and Ni-CNT have no catalytic activity for CO_2 reduction to CO, indicating that Ni nanoparticles have a preference for the HER over the CO_2RR. These results are consistent with previous reports from Boppella et al. [50]. It is worth noting that although the ANBC shows good faradaic efficiency toward CO, the j_{CO} of ANBC is much lower than that of Ni-N-ANBC, indicating that ANBC alone has a relatively poor activity for CO_2 reduction to CO. This implies that the primary activity of Ni-N-ANBC is provided by the Ni-N_x moieties on the ANBC, rather than the N-doped biochar itself. The contribution of the active sites on ANBC to the overall activity of Ni-N-ANBC is almost negligible.

Longer-term (8 h) stability measurements of Ni-N-C catalysts were performed at −0.9 V vs. RHE (Fig. 3e). Ni-N-CNT and Ni-N-ANBC are stable and show only a small decrease of 5 % FE_{CO} after 8 h of electrolysis, while the FE_{CO} of Ni-N-CB decreases from ~90 % to ~75 %. The current density of all Ni-N-C catalysts exhibits a decreasing trend over the first 2 h, which is attributed to the detachment of the catalysts, and then maintains stable performance. Hu et al. observed a similar detachment phenomenon for their metal-nitrogen-carbon based catalysts [19]. In general, Ni-N-CNT and Ni-N-ANBC show a higher catalytic activity and longer stability during electrochemical CO_2 reduction than Ni-N-CB.

To study the structure-performance relationship of the Ni-N-C catalysts, several electrochemical characterizations were performed. The electrochemical active surface areas (ECSA) of all prepared samples were determined by measuring the electric double-layer capacitances (C_{dl}) (Figure S11). As shown in Fig. 4a, Ni-N-ANBC (0.93 mF/cm^2) shows a significantly larger C_{dl} value than Ni-N-CB (0.26 mF/cm^2) and Ni-N-CNT (0.36 mF/cm^2). The C_{dl} values of these Ni-N-C catalysts are positively correlated with their specific surface areas which are calculated by N_2 adsorption-desorption measurements. However, the obtained C_{dl} values do not show a clear correlation with their electrochemical performances. Although the C_{dl} values of Ni-N-CNT and Ni-N-ANBC display significant differences, their electrocatalytic performances for CO_2RR are similar. In addition, despite the Ni-C samples showing no CO_2RR activity or less CO_2RR activity than the Ni-N-C catalysts, the C_{dl} values of the Ni-C samples are similar to those of the Ni-N-C catalysts (Figure S12), which indicates that the C_{dl} values are mainly dependent on the properties of carbon supports rather than the active sites. This means that not all electrochemically active sites are catalytically active for the CO_2RR. Therefore, in the case of porous carbon-based catalysts, we believe that ECSA-based calculations are not effective in comparing their catalytic performances.

Electrochemical impedance spectroscopy (EIS) measurement results are depicted in Fig. 4b. The semicircles in mid-frequency region show that Ni-N-CNT and Ni-N-ANBC exhibit lower charge-transfer resistance than Ni-N-CB, indicating faster electron transfer during the CO_2RR. In low-frequency region, Ni-N-ANBC exhibits a smaller semicircle than Ni-N-CNT and Ni-N-CB, indicating a faster diffusion process on Ni-N-ANBC. The improvement in mass transfer may be attributed to the unique porous structure of ANBC. Control measurements with the Ni-C samples (Figure S13) show similar charge-transfer resistances to that of the Ni-N-C catalysts, indicating that the charge-transfer resistances are determined by the properties of the carbon supports. The kinetics of the Ni-N-C catalysts are plotted in Tafel slopes (Fig. 4c). The Tafel slope values of Ni-N-CB, Ni-N-CNT, and Ni-N-ANBC are calculated to be 130, 157, and 133 mV/dec, respectively. All of these values are close to the theoretical value of 118 mV/dec, implying that the prepared Ni-N-C catalysts have a similar rate-determining step (RDS) toward CO_2RR, which is the first single electron transfer step of adsorbed CO_2 to a $CO_2^{\cdot-}$ intermediate [51–53].

Control experiments to verify whether the observed CO was produced from CO_2 were carried out in an Ar-saturated electrolyte at −0.9 V vs. RHE. As shown in Figure S14, the carbon paper used as substrate for electrode preparation shows a low catalytic activity and only produces H_2 in both CO_2-saturated and Ar-saturated electrolytes, suggesting that all of the CO_2RR activity is derived from the Ni-N-C catalysts. Performing chronoamperometry measurements with the Ni-N-C catalysts in an Ar-saturated electrolyte only leads to H_2 production, indicating that all of the produced CO originates from electrochemical CO_2 reduction and not from the decomposition of the carbon supports.

3.3. Factors behind the performance differences

The hydrophobicity and surface roughness of porous carbon electrocatalysts are considered to have a critical impact on their performance for the CO_2RR [54]. A more hydrophobic surface helps to inhibit the HER and thereby enhances the CO_2RR performance [55]. The surface roughness affects the residence time of gas bubbles on the electrode surface [56]. Bubbles with a larger size and longer residence time can partially cover the active sites resulting in a lower activity [57]. In this study, we carried out static contact angle measurements to evaluate the hydrophobicity of the Ni-N-C catalysts, with a larger contact angle indicating a higher hydrophobicity. Dynamic contact angle (advancing-receding contact angle) measurements were performed to evaluate the surface roughness of the drop-casted electrodes. In particular, as the electrode surface becomes rougher, the difference between the advancing contact angle and receding contact angle becomes larger, conversely, the difference in the diameter of the drop base becomes smaller. The results of hydrophobicity and surface roughness of Ni-N-C catalysts are depicted in Figure S15. All Ni-N-C catalysts show contact angles around 130° (Figure S15a and Table S2), indicating that they possess similar hydrophobicity. In addition, the difference between advancing and receding contact angles (Figure S15b) and the difference in diameters of the drop base (Figure S15c) of all Ni-N-C catalysts are almost negligible, suggesting that all of them show a similar surface roughness. Accordingly, the macroscopic surface properties (hydrophobicity and surface roughness) does not explain the difference in CO_2RR performance.

Porous carbon-based catalysts can improve the CO_2RR electrocatalytic performance [58]. Abundant porous structures provide a larger specific surface area, while mesopores and macropores play an important role in enhancing the mass transfer and improving the accessibility of the active sites [59]. N_2 adsorption-desorption measurements were performed to determine the specific surface area and porosity of the prepared Ni-N-C catalysts. The N_2 adsorption-desorption isotherms of Ni-N-C catalysts are shown in Fig. 5a, with the curves of Ni-N-CB and Ni-N-CNT exhibiting a rapid increase at relatively high pressures (P/P_0

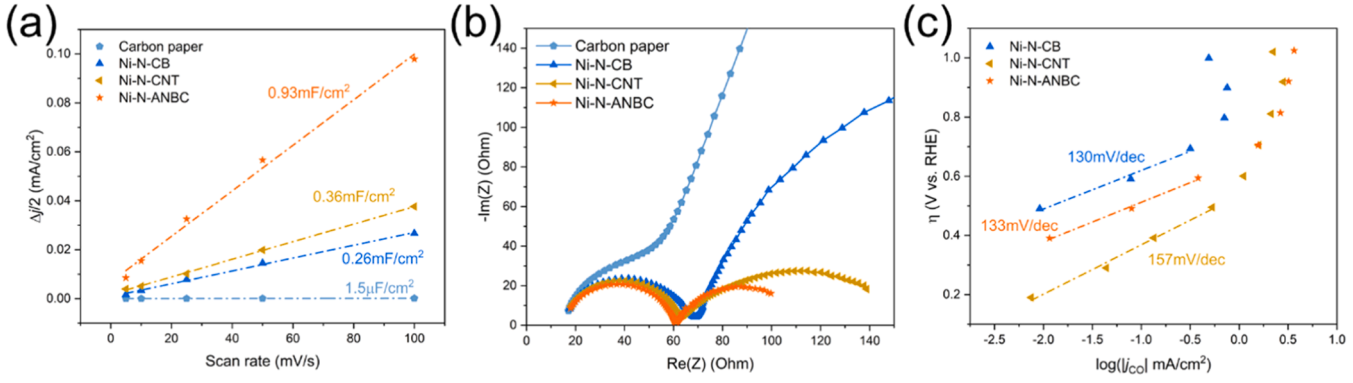

Fig. 4. (a) Double layer capacitance, (b) Nyquist plots, and (c) Tafel plots of Ni-N-CB, Ni-N-CNT, and Ni-N-ANBC.

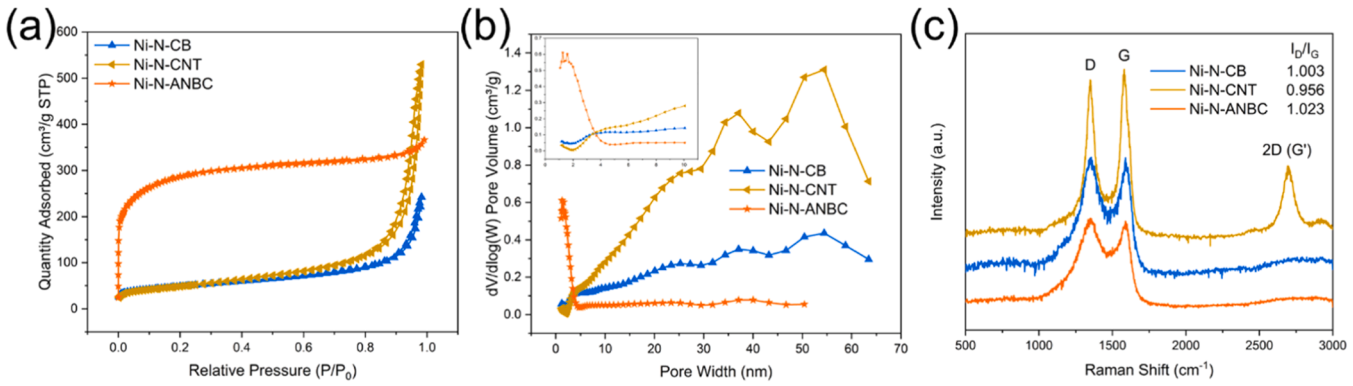

Fig. 5. (a) N_2 adsorption-desorption isotherms, (b) Pore width distributions, (c) Raman spectra of Ni-N-CB, Ni-N-CNT, and Ni-N-ANBC.

> 0.8), suggesting the presence of macropores. Additionally, Ni-N-CNT shows an apparent hysteresis loop ($0.8 < P/P_0 < 1.0$), indicating the existence of mesopores. On the contrary, Ni-N-ANBC exhibits a sharp uptake at relatively low pressures ($P/P_0 < 0.005$), revealing the predominant presence of micropores. The corresponding pore width distributions of Ni-N-C catalysts (Fig. 5b), which are calculated by a density functional theory (DFT) model gives detailed results. The pore width of Ni-N-CB and Ni-N-ANBC are mainly centered around 55 nm and 2 nm, respectively. However, the pore width distribution of Ni-N-CNT shows two intensive peaks located at 35 nm and 55 nm. The specific surface areas of Ni-N-CB, Ni-N-CNT, and Ni-N-ANBC are calculated to be 171.4 m^2/g, 173.3 m^2/g, and 1053.5 m^2/g, respectively. The percentage of meso- and macropores of Ni-N-CB, Ni-N-CNT, and Ni-N-ANBC are 94.4 %, 99.0 %, and 26.0 %, respectively (Table S3). It is noteworthy that although Ni-N-CNT and Ni-N-ANBC show substantial differences in specific surface area and the percentage of meso-/macropores, they show similar CO_2RR performances. This indicates that the contribution of micropores in carbon materials should not be underestimated. Micropores provide large specific surface area and improve the dispersion of the active sites, which could significantly improve the catalytic performance for CO_2RR. This is in line with the literature, where Estevez et al. reported that a higher percentage of micropores in carbon materials can enhance the CO_2 capture performance [60], while Liu et al. synthesized a coal-based N-doped carbon catalyst for CO_2RR and pointed out that the spatial confinement effect of the micropores is beneficial for CO_2 conversion to CO [61]. Furthermore, the N_2 adsorption-desorption isotherms, pore width distribution, and textural properties of pristine carbon materials and Ni-C samples are summarized in Figure S16 and Table S3. It can be clearly seen that the isotherms and pore width distributions of pristine carbon materials and Ni-C samples are similar to the Ni-N-C catalysts. Loading Ni or Ni-N_x onto the carbon support blocks part of the pores and leads to a decrease in specific surface area (Table S3), but does not change the main porosity of the carbon material itself. These results demonstrate that the ligand-mediated synthesis method for Ni-N-C catalysts does not affect the pristine porosity of the carbon supports.

A trade-off between conductivity and defects in carbon-based catalysts also influences their performances. Better electrical conductivity of the carbon supports can enhance electron transfer, while abundant defects in carbon materials have also been demonstrated to facilitate the adsorption and activation of CO_2 [62]. Hence, Raman spectroscopy is carried out to analyze the degree of graphitization and the abundance of defects of Ni-N-C catalysts. As shown in Fig. 5c, all of the materials show two peaks located at around 1350 cm^{-1} and 1590 cm^{-1} that can be assigned as the D band and G band of carbon materials. The lower I_D/I_G ratio reflects the higher degree of graphitization and less defects in carbon materials, vice versa. Ni-N-CNT shows the lowest I_D/I_G value, indicating its high degree of graphitization. Additionally, Ni-N-CNT displays another distinct peak at around 2700 cm^{-1}, which can be attributed to the 2D band of graphitic carbon materials, indicating that Ni-N-CNT has a better electrical conductivity. Furthermore, the Raman spectroscopy results are consistent with the X-ray photoelectron spectrometry (XPS) results (Table S1). The carbon content of Ni-N-CNT is higher than that of Ni-N-CB and Ni-N-ANBC, indicating fewer heteroatoms or functional groups on the catalyst. This also supports the conclusion that Ni-N-CNT has better conductivity than the other two catalysts. The better conductivity should be the main reason that Ni-N-CNT shows a lower onset potential and exhibits higher current density and faradaic efficiency at less negative potentials compared to Ni-N-CB and Ni-N-ANBC.

As for the abundance of defects, Ni-N-ANBC ($I_D/I_G = 1.023$) exhibits more defects than Ni-N-CB ($I_D/I_G = 1.003$) and Ni-N-CNT ($I_D/I_G = 0.956$), which is attributed to the introduced nitrogen heteroatoms. However, both Ni-N-ANBC and Ni-N-CNT show similar performances toward the CO_2RR, suggesting that the contributions of defects in Ni-N-C catalysts to CO_2RR activity are almost negligible. It is important to note that several studies have demonstrated that the intrinsic defects in carbon materials show efficient catalytic activity for CO_2RR [63–65]. However, most of the reported defect-rich carbon materials are generated by the removal of nitrogen heteroatoms from N-doped carbon via thermal treatment under an inert atmosphere [66]. Nonetheless, high temperatures can not completely remove the nitrogen heteroatoms and also facilitate carbon network rearrangements leading to a decrease in defects [67,68]. Therefore, it is difficult to assess the contribution of defects in carbon supports of Ni-N-C catalysts to CO_2RR performance. Furthermore, the Raman spectra of pristine carbon materials and Ni-C samples are depicted in Figure S17. All of the Ni-N-C catalysts and Ni-C samples show lower I_D/I_G values than the pristine carbon materials, indicating that the additional annealing and introduction of other carbon sources (1,10 - phenanthroline) will decrease the abundance of defects in carbon supports and improve their degree of graphitization.

Apart from the contribution of porosity to the CO_2RR performance, the distribution of Ni-N_x active sites has a crucial influence on the CO_2RR performances of Ni-N-C catalysts. This distribution is jointly affected by the morphology and porosity of different carbon supports [69,70]. The Ni loadings of different Ni-N-C catalysts were measured by both XPS and inductively coupled plasma optical emission spectrometry (ICP-OES). For comparison, the XPS results in atomic percentages (at%) were converted to weight percentages (wt%). As shown in Fig. 6a, the ICP-OES results indicate that all Ni-N-C catalysts show a similar Ni loading at around 1.1 wt%, close to the intended Ni loading of 1.5 wt%. However, XPS results show that the contents of Ni in Ni-N-CB, Ni-N-CNT, and Ni-N-ANBC are 0.24 wt%, 0.51 wt%, and 0.32 wt%, respectively, which are lower than the results obtained by ICP-OES analysis. This difference attests that part of the Ni-N_x active sites are confined inside the pores of the different carbon supports and are therefore not detectable by XPS. Since the penetration depth of XPS is limited and only reflects the Ni content on the surface of Ni-N-C catalysts

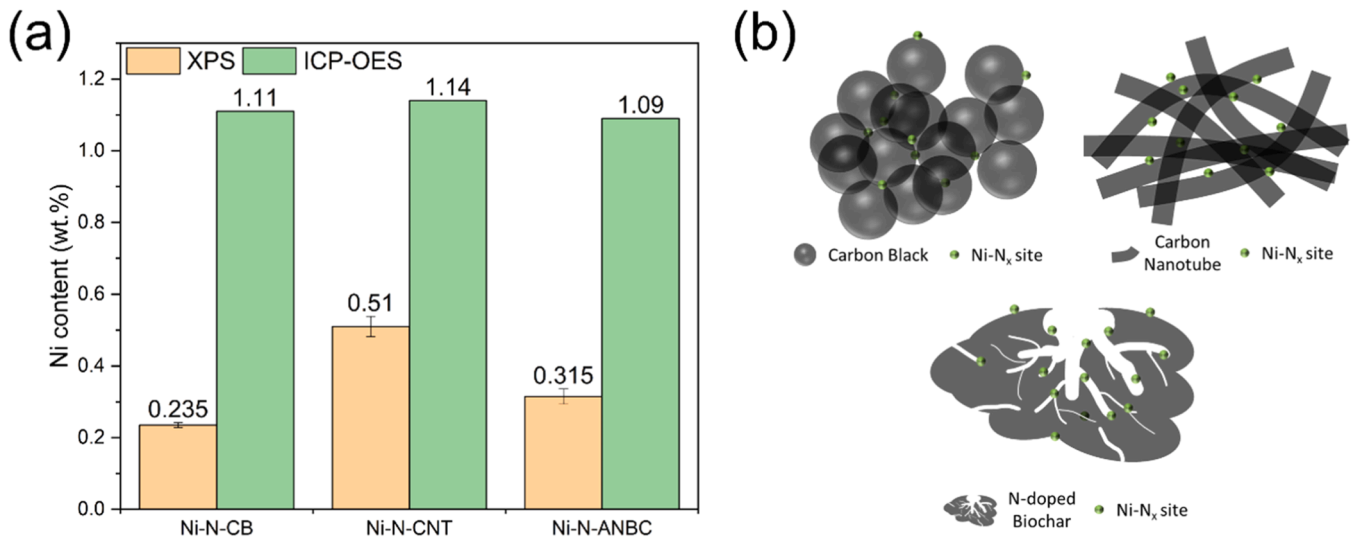

Fig. 6. (a) The Ni content of Ni-N-CB, Ni-N-CNT, and Ni-N-ANBC quantified by XPS and ICP. (b) Schematic illustration of the distribution of actives of Ni-N-CB, Ni-N-CNT, and Ni-N-ANBC.

[71], the results of the XPS analysis indicate that Ni-N-CNT has more surface Ni-N_x active sites than Ni-N-CB and Ni-N-ANBC. Combining the different distributions of active sites, structural properties and electrochemical performances of Ni-N-C catalysts, we illustrate our findings in Fig. 6b. Due to the agglomeration of carbon black nanospheres, parts of Ni-N_x sites are buried inside of stacked carbon black nanoparticles. Therefore, the Ni-N-CB catalyst shows a lower CO_2RR current density compared to Ni-N-CNT and Ni-N-ANBC. On the contrary, due to the fiber-like, the multilayered tubular structure of the multi-walled carbon nanotube, the Ni-N_x active sites cannot easily enter the interior of the carbon nanotube. By virtue of its abundant surface Ni-N_x active sites and wider pore size, Ni-N-CNT exhibits better CO_2RR performances than other Ni-N-C catalysts at relatively lower overpotentials. In contrast, Ni-N-ANBC has a hierarchical structure and a part of the Ni-N_x active sites are distributed in deeper and smaller pores. This leads to some Ni-N_x sites not being readily accessible and showing a poorer CO_2RR activity at more positive potentials. However, as the potential becomes more negative, electrowetting helps to improve the accessibility of Ni-N_x active sites in the pores of the ANBC [72]. Consequently, this distribution of active sites allows the Ni-N-ANBC catalyst to maintain a good FE_{CO} (> 90 %) and j_{CO} at more negative potentials.

From the above discussions, we find that the CO_2RR performances of the Ni-N-C catalysts are highly dependent on the applied carbon supports. The agglomeration of carbon black nanospheres covers several Ni-N_x active sites, which causes Ni-N-CB to show a relatively poor CO_2RR performance. Multi-walled carbon nanotubes display larger pore sizes than other carbon supports and the Ni-N_x active sites are mostly distributed on the surface of carbon nanotubes. This allows fast mass transfer of reactants to the active sites, thus enabling Ni-N-CNT to show excellent CO_2RR performance even at low overpotential. On the contrary, N-doped biochar shows a hierarchical structure with a large number of micropores, where part of the Ni-N_x active sites are confined in deeper and smaller pores. This enables Ni-N-ANBC to exhibit a great CO_2RR performance at more negative potentials. In general, we can therefore conclude that selecting a suitable carbon support is important to help Ni-N-C catalysts exhibit better CO_2RR performances.

3.4. Carbon support effects on CO_2 reduction at high current densities

Owing to the low solubility of CO_2 in aqueous solutions and the resulting mass transfer limitation in the H-cell configuration, the overall currents are limited and the differences in current density of the Ni-N-C catalysts are a few milliamperes. To investigate the importance of carbon supports for the Ni-N-C catalysts at high current densities, CO_2RR experiments were carried out in a MEA-type electrolysis system. Due to the porous structure of the gas diffusion layer, the CO_2 diffusion path to the surface of catalyst is around three orders of magnitude smaller than conventional non-GDE system, which enables significantly higher current densities. Moreover, the zero-gap configuration can greatly reduce ohmic resistances. By utilizing the MEA cell for CO_2RR, high current densities (> 100 mA/cm^2) could easily be achieved. In this study, the Ni-N-C catalysts were spray coated on a gas diffusion layer with a loading of 0.5 mg/cm^2, humidified CO_2 was supplied to the cathode compartment through a serpentine flow channel and a 1 M $KHCO_3$ solution was circulated to the anode side where the oxygen evolution reaction takes place. The electrocatalytic activity of the Ni-N-C catalysts was investigated by applying constant current densities ranging from 25 to 200 mA/cm^2 in a stepwise manner. The cell potential was recorded at each current density as a function of time.

The FEs as a function of current density of Ni-N-C catalysts show similar trends, where the FE_{CO} is over 90 % from 25 to 150 mA/cm^2 and slightly decreases at 200 mA/cm^2 (Fig. 7a, b, c). The FE_{CO} achieves the maximum value of 97.7 %, 97.8 %, and 98.3 % at 100 mA/cm^2 for Ni-N-CB, Ni-N-CNT, and Ni-N-ANBC, respectively. The FE_{H2} of Ni-N-CNT (20.8 %) at 200 mA/cm^2 is higher than that of Ni-N-CB (10.2 %) and Ni-N-ANBC (10.4 %). This is in line with the results observed in the H-cell measurements (Figure S9b), where the Ni-N-CNT catalyst shows a relatively larger HER activity than Ni-N-CB and Ni-N-ANBC at more negative potentials. Despite the fact that the faradaic efficiency distributions are similar for all catalysts, the cell voltages for the different catalysts show significant differences (Fig. 7d). Ni-N-CB shows a higher cell voltage than Ni-N-CNT and Ni-N-ANBC at all tested current densities. This is consistent with the relatively poor catalytic activity of Ni-N-CB that was observed in the H-cell experiments. Ni-N-CNT shows a lower cell voltage than Ni-N-CB and Ni-N-ANBC at 25 mA/cm^2. It is worth noting that as the current density increases, the cell potentials of Ni-N-ANBC at higher current densities (> 100 mA/cm^2) are even lower than Ni-N-CNT, indicating that Ni-N-ANBC shows better catalytic activity than Ni-N-CNT at more negative potentials, which is in accordance with the H-cell results. This is mainly attributed to the hierarchically porous structure and larger specific surface area of ANBC and abundant Ni-N_x active sites inside the pores, which facilitates the mass diffusion and improves the accessibility of active sites. We observe a significant increase in cell potential during the 100–125 minute interval at

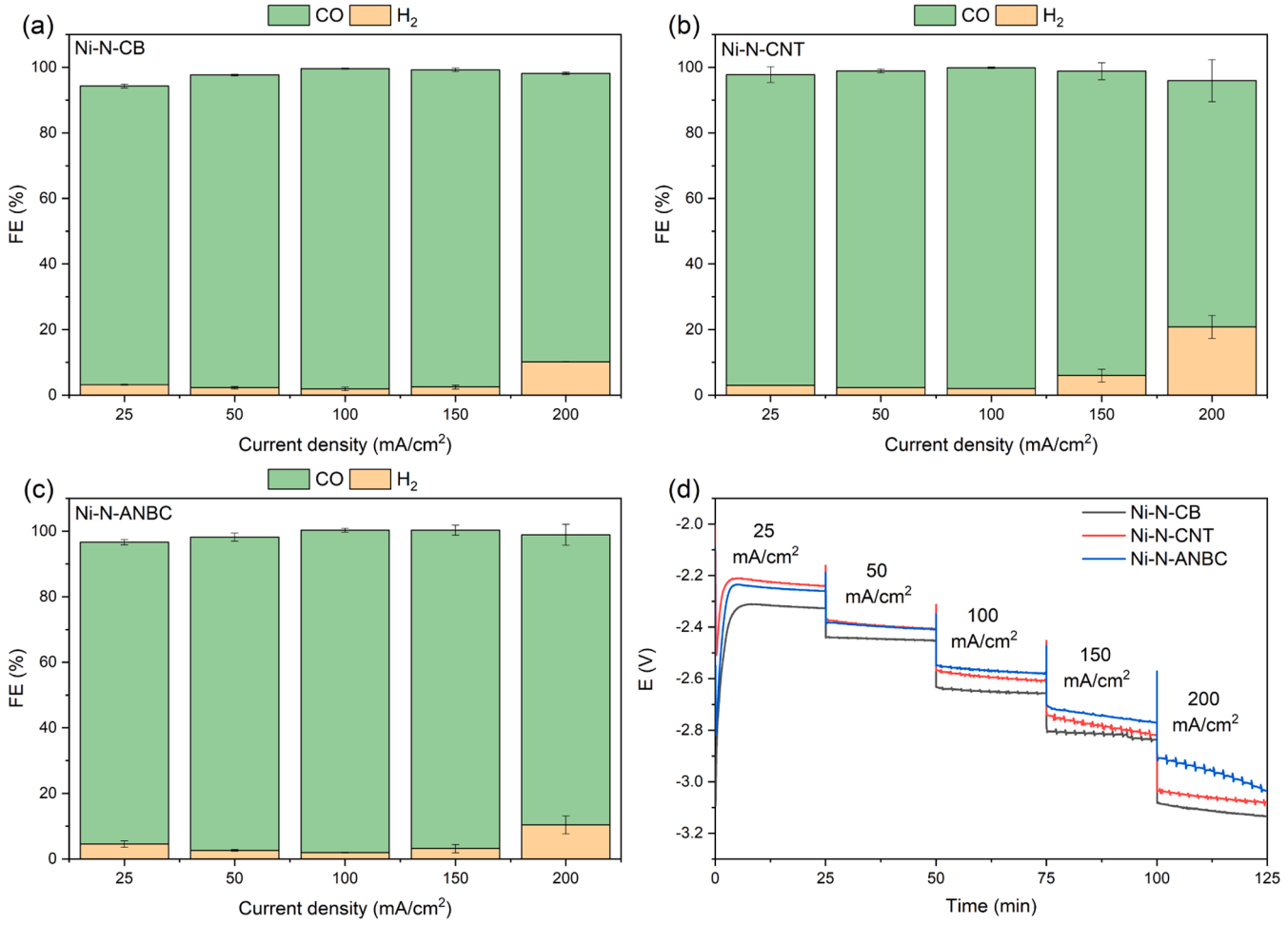

Fig. 7. Faradaic efficiency as a function of current density of (a) Ni-N-CB, (b) Ni-N-CNT, (c) Ni-N-ANBC; (d) Cell voltage at different current densities of different Ni-N-C catalysts.

200 mA/cm^2 (Fig. 7d), which is attributed to the effects of salt formation on the GDE (Figure S18). After removing the accumulated salt, the performance of the catalyst can be restored (Figure S19).

A series of post-reaction characterizations were conducted to evaluate the stability of the Ni-N_x active sites, including SEM, TEM, and XPS analyses. The SEM images confirmed that there were no significant changes in the morphology of the catalysts (Figure S20). TEM images further showed that no obvious Ni nanoparticles formed after the reaction (Figure S20). Additionally, the XPS spectra indicated that the valence states of the Ni species remained unchanged, suggesting that the active sites remained stable during the reaction (Figure S21). These findings demonstrate that these Ni-N-C catalysts maintain their structural and chemical properties after electrochemical measurements, confirming that the performance decrease is due to salt formation rather than the degradation of the Ni-N_x active sites.

In summary, these findings clearly point out that the properties of the carbon support for the CO_2RR performance of Ni-N-C catalysts are important, both in the H-cell and at higher current densities in the MEA cell. The textural properties of the carbon supports and the distribution of Ni-N_x active sites play dominant role in the electrocatalytic performance for CO_2RR to CO.

4. Conclusions

We have successfully synthesized a group of Ni-N-C catalysts by using different carbon supports via a ligand-mediated method. These prepared Ni-N-C catalysts were initially tested in an H-cell. We comprehensively studied the critical factors of carbon supports that govern the CO_2RR performances of the prepared Ni-N-C catalysts, which include hydrophobicity, surface roughness, porosity, the abundance of defects, and the distribution of active sites. All of the Ni-N-C catalysts exhibit a similar hydrophobicity and surface roughness and show high faradaic efficiencies toward CO (ca. 90 %) over different potential windows. However, their partial current densities show significant differences. We find that the morphology and porosity of different carbon supports influences the distribution and accessibility of the Ni-N_x active sites. As a result, Ni-N-CB shows a relatively poor CO_2RR performances, that is attributed to the agglomeration of carbon black nanospheres which covers parts of Ni-N_x active sites. Ni-N-CNT displays a wider pore size and more Ni-N_x active sites on the carbon surface, which enables faster mass transfer of reactants to the Ni-N_x active sites, enabling the Ni-N-CNT to show a great FE_{CO} (>90 %) and j_{CO} at lower overpotentials. The micropore-dominated N-doped biochar with hierarchical porous structures exhibits a larger specific surface area and smaller pore size, with part of the Ni-N_x active sites confined in deeper and narrower pores. This pore architecture enables Ni-N-ANBC to maintain a good FE_{CO} even at more negative potentials. Furthermore, high current CO_2RR measurements (25–200 mA/cm^2) were carried out in an MEA system. Here, Ni-N-CB showed a relatively poorer catalytic performance than Ni-N-CNT and Ni-N-ANBC. Benefiting from the hierarchical porous structure and the distribution of Ni-N_x active sites, Ni-N-ANBC shows a lower cell voltage than Ni-N-CNT and Ni-N-CB from 50 to 200 mA/cm^2. Overall, this study reveals the role of carbon support of Ni-N-C catalysts and presents the importance of selecting suitable carbon supports for Ni-

N-C catalysts to exhibit an excellent CO_2RR performance.

CRediT authorship contribution statement

Qi An: Investigation, Data curation. **Min Li:** Investigation, Data curation. **Wiebren de Jong:** Writing – review & editing, Supervision, Methodology, Funding acquisition. **Ruud Kortlever:** Writing – review & editing, Supervision, Funding acquisition, Conceptualization. **Shilong Fu:** Writing – review & editing, Writing – original draft, Visualization, Validation, Methodology, Investigation, Formal analysis, Data curation. **Boaz Izelaar:** Writing – review & editing, Methodology, Investigation, Data curation. **Ming Li:** Methodology, Investigation, Data curation.

Declaration of Competing Interest

The authors declare that they have no known competing financial interests or personal relationships that could have appeared to influence the work reported in this paper.

Acknowledgement

Shilong Fu, Ming Li, Qi An, and Min Li acknowledge the PhD scholarship awarded by China Scholarship Council (CSC). Boaz Izelaar and Ruud Kortlever acknowledge the Nitrogen Activation and Ammonia Oxidation project within the Electron to Chemical Bonds consortium with project number P17–08, which is financed by The Netherlands Organization for Scientific Research (NWO) and affiliated industrial partners. The authors thank Michel van den Brink for help in performing the experiments.

Appendix A. Supporting information

Supplementary data associated with this article can be found in the online version at doi:10.1016/j.nanoen.2024.110461.

Data Availability

Data will be made available on request.

References

[1] S. Chu, Y. Cui, N. Liu, The path towards sustainable energy, Nat. Mater. 16 (2017) 16–22, https://doi.org/10.1038/NMAT4834.
[2] B. Obama, The irreversible momentum of clean energy, Science 355 (2017) 126–129, https://doi.org/10.1126/science.aam6284.
[3] R. Kortlever, J. Shen, K.J.P. Schouten, F. Calle-Vallejo, M.T.M. Koper, Catalysts and reaction pathways for the electrochemical reduction of carbon dioxide, J. Phys. Chem. Lett. 6 (2015) 4073–4082, https://doi.org/10.1021/acs.jpclett.5b01559.
[4] Y.Y. Birdja, E. Pérez-Gallent, M.C. Figueiredo, A.J. Göttle, F. Calle-Vallejo, M.T. M. Koper, Advances and challenges in understanding the electrocatalytic conversion of carbon dioxide to fuels, Nat. Energy 4 (2019) 732–745, https://doi.org/10.1038/s41560-019-0450-y.
[5] Z.W. Seh, J. Kibsgaard, C.F. Dickens, I.B. Chorkendorff, J.K. Nørskov, T. F. Jaramillo, Combining theory and experiment in electrocatalysis: insights into materials design, Science 355 (2017) eaad4998, https://doi.org/10.1126/science.aad4998.
[6] P. De Luna, C. Hahn, D. Higgins, S.A. Jaffer, T.F. Jaramillo, E.H. Sargent, What would it take for renewably powered electrosynthesis to displace petrochemical processes? Science 364 (2019) eaav3506 https://doi.org/10.1126/science.aav3506.
[7] K.R. Lawrence, A.S. Kumar, S. Asperti, D. van den Berg, N. Girichandran, R. KortleverAdvances in Electrochemical Carbon Dioxide Reduction Toward Multi-carbon Products, in: Chem. Valoris. Carbon Dioxide, 2022: pp. 388–412. 2022, https://doi.org/10.1039/9781839167645-00388.
[8] S. Jin, Z. Hao, K. Zhang, Z. Yan, J. Chen, Advances and challenges for the electrochemical reduction of CO_2 to CO: from fundamentals to industrialization, Angew. Chem. Int. Ed. 133 (2021) 20627–20648, https://doi.org/10.1002/anie.202101818.
[9] K. Van Daele, B. De Mot, M. Pupo, N. Daems, D. Pant, R. Kortlever, T. Breugelmans, Sn-based electrocatalyst stability: a crucial piece to the puzzle for the electrochemical CO_2 reduction toward formic acid, ACS Energy Lett. 6 (2021) 4317–4327, https://doi.org/10.1021/ACSENERGYLETT.1C02049.
[10] A. Guan, Z. Chen, Y. Quan, C. Peng, Z. Wang, T.-K. Sham, C. Yang, Y. Ji, L. Qian, X. Xu, Boosting CO_2 electroreduction to CH_4 via tuning neighboring single-copper sites, ACS Energy Lett. 5 (2020) 1044–1053, https://doi.org/10.1021/acsenergylett.0c00018.
[11] C.-T. Dinh, T. Burdyny, M.G. Kibria, A. Seifitokaldani, C.M. Gabardo, F.P.G. De Arquer, A. Kiani, J.P. Edwards, P. De Luna, O.S. Bushuyev, CO_2 electroreduction to ethylene via hydroxide-mediated copper catalysis at an abrupt interface, Science 360 (2018) 783–787, https://doi.org/10.1126/science.aas9100.
[12] T. Zheng, K. Jiang, H. Wang, Recent advances in electrochemical CO_2-to-CO conversion on heterogeneous catalysts, Adv. Mater. 30 (2018) 1802066, https://doi.org/10.1002/adma.201802066.
[13] D.L.T. Nguyen, Y. Kim, Y.J. Hwang, D.H. Won, Progress in development of electrocatalyst for CO_2 conversion to selective CO production, Carbon Energy 2 (2020) 72–98, https://doi.org/10.1002/cey2.27.
[14] S. Hernández, M.A. Farkhondehfal, F. Sastre, M. Makkee, G. Saracco, N. Russo, Syngas production from electrochemical reduction of CO_2: current status and prospective implementation, Green. Chem. 19 (2017) 2326–2346, https://doi.org/10.1039/C7GC00398F.
[15] S. Zhao, R. Jin, R. Jin, Opportunities and challenges in CO_2 reduction by gold-and silver-based electrocatalysts: from bulk metals to nanoparticles and atomically precise nanoclusters, ACS Energy Lett. 3 (2018) 452–462, https://doi.org/10.1021/acsenergylett.7b01104.
[16] A.S. Varela, N. Ranjbar Sahraie, J. Steinberg, W. Ju, H.S. Oh, P. Strasser, Metal-doped nitrogenated carbon as an efficient catalyst for direct CO_2 electroreduction to CO and hydrocarbons, Angew. Chem. Int. Ed. 54 (2015) 10758–10762, https://doi.org/10.1002/anie.201502099.
[17] P. Brimley, H. Almajed, Y. Alsunni, A.W. Alherz, Z.J.L. Bare, W.A. Smith, C. B. Musgrave, Electrochemical CO_2 reduction over metal-/nitrogen-doped graphene single-atom catalysts modeled using the grand-canonical density functional theory, ACS Catal. 12 (2022) 10161–10171, https://doi.org/10.1021/acscatal.2c01832.
[18] W. Ju, A. Bagger, G.P. Hao, A.S. Varela, I. Sinev, V. Bon, B. Roldan Cuenya, S. Kaskel, J. Rossmeisl, P. Strasser, Understanding activity and selectivity of metal-nitrogen-doped carbon catalysts for electrochemical reduction of CO_2, Nat. Commun. 8 (2017) 944, https://doi.org/10.1038/s41467-017-01035-z.
[19] X.M. Hu, H.H. Hval, E.T. Bjerglund, K.J. Dalgaard, M.R. Madsen, M.M. Pohl, E. Welter, P. Lamagni, K.B. Buhl, M. Bremholm, M. Beller, S.U. Pedersen, T. Skrydstrup, K. Daasbjerg, Selective CO_2 reduction to CO in water using earth-abundant metal and nitrogen-doped carbon electrocatalysts, ACS Catal. 8 (2018) 6255–6264, https://doi.org/10.1021/ACSCATAL.8B01022.
[20] F. Pan, W. Deng, C. Justiniano, Y. Li, Identification of champion transition metals centers in metal and nitrogen-codoped carbon catalysts for CO_2 reduction, Appl. Catal. B Environ. 226 (2018) 463–472, https://doi.org/10.1016/j.apcatb.2018.01.001.
[21] J. Li, P. Pršlja, T. Shinagawa, A.J. Martín Fernández, F. Krumeich, K. Artyushkova, P. Atanassov, A. Zitolo, Y. Zhou, R. García-Muelas, N. López, J. Pérez-Ramírez, F. Jaouen, Volcano trend in electrocatalytic CO_2 reduction activity over atomically dispersed metal sites on nitrogen-doped carbon, ACS Catal. 9 (2019) 10426–10439, https://doi.org/10.1021/ACSCATAL.9B02594.
[22] T. Möller, W. Ju, A. Bagger, X. Wang, F. Luo, T.N. Thanh, A.S. Varela, J. Rossmeisl, P. Strasser, Efficient CO_2 to CO electrolysis on solid Ni–N–C catalysts at industrial current densities, Energy Environ. Sci. 12 (2019) 640–647, https://doi.org/10.1039/C8EE02662A.
[23] T. Zheng, K. Jiang, N. Ta, Y. Hu, J. Zeng, J. Liu, H. Wang, Large-scale and highly selective CO_2 electrocatalytic reduction on nickel single-atom catalyst, Joule 3 (2019) 265–278, https://doi.org/10.1016/J.JOULE.2018.10.015.
[24] Z. Wang, J. Choi, M. Xu, X. Hao, H. Zhang, Z. Jiang, M. Zuo, J. Kim, W. Zhou, X. Meng, Optimizing electron densities of Ni-N-C complexes by hybrid coordination for efficient electrocatalytic CO_2 reduction, ChemSusChem 13 (2020) 929–937, https://doi.org/10.1002/cssc.201903427.
[25] K. Mou, Z. Chen, X. Zhang, M. Jiao, X. Zhang, X. Ge, W. Zhang, L. Liu, Highly efficient electroreduction of CO_2 on nickel single-atom catalysts: atom trapping and nitrogen anchoring, Small 15 (2019) 1903668, https://doi.org/10.1002/smll.201903668.
[26] X. Li, W. Bi, M. Chen, Y. Sun, H. Ju, W. Yan, J. Zhu, X. Wu, W. Chu, C. Wu, Exclusive Ni–N_4 sites realize near-unity CO selectivity for electrochemical CO_2 reduction, J. Am. Chem. Soc. 139 (2017) 14889–14892, https://doi.org/10.1021/jacs.7b09074.
[27] J. Yang, Z. Qiu, C. Zhao, W. Wei, W. Chen, Z. Li, Y. Qu, J. Dong, J. Luo, Z. Li, In situ thermal atomization to convert supported nickel nanoparticles into surface-bound nickel single-atom catalysts, Angew. Chem. Int. Ed. 57 (2018) 14095–14100, https://doi.org/10.1002/anie.201808049.
[28] C. Yan, H. Li, Y. Ye, H. Wu, F. Cai, R. Si, J. Xiao, S. Miao, S. Xie, F. Yang, Y. Li, G. Wang, X. Bao, Coordinatively unsaturated nickel-nitrogen sites towards selective and high-rate CO_2 electroreduction, Energy Environ. Sci. 11 (2018) 1204–1210, https://doi.org/10.1039/c8ee00133b.
[29] A.S. Varela, W. Ju, A. Bagger, P. Franco, J. Rossmeisl, P. Strasser, Electrochemical Reduction of CO_2 on metal-nitrogen-doped carbon catalysts, ACS Catal. 9 (2019) 7270–7284, https://doi.org/10.1021/ACSCATAL.9B01405.
[30] Y. Niu, C. Zhang, Y. Wang, D. Fang, L. Zhang, C. Wang, Confining chainmail-bearing Ni nanoparticles in N-doped carbon nanotubes for robust and efficient electroreduction of CO_2, ChemSusChem 14 (2021) 1140–1154, https://doi.org/10.1002/cssc.202002596.
[31] K. Jiang, S. Siahrostami, T. Zheng, Y. Hu, S. Hwang, E. Stavitski, Y. Peng, J. Dynes, M. Gangisetty, D. Su, Isolated Ni single atoms in graphene nanosheets for high-performance CO_2 reduction, Energy Environ. Sci. 11 (2018) 893–903, https://doi.org/10.1039/C7EE03245E.

[32] K. Jiang, S. Siahrostami, A.J. Akey, Y. Li, Z. Lu, J. Lattimer, Y. Hu, C. Stokes, M. Gangishetty, G. Chen, Transition-metal single atoms in a graphene shell as active centers for highly efficient artificial photosynthesis, Chem 3 (2017) 950–960, https://doi.org/10.1016/j.chempr.2017.09.014.

[33] P. Lu, Y. Yang, J. Yao, M. Wang, S. Dipazir, M. Yuan, J. Zhang, X. Wang, Z. Xie, G. Zhang, Facile synthesis of single-nickel-atomic dispersed N-doped carbon framework for efficient electrochemical CO_2 reduction, Appl. Catal. B Environ. 241 (2019) 113–119, https://doi.org/10.1016/J.APCATB.2018.09.025.

[34] H.-Y. Jeong, M. Balamurugan, V.S.K. Choutipalli, E. Jeong, V. Subramanian, U. Sim, K.T. Nam, Achieving highly efficient CO_2 to CO electroreduction exceeding 300 mA cm^{-2} with single-atom nickel electrocatalysts, J. Mater. Chem. A. 7 (2019) 10651–10661, https://doi.org/10.1039/C9TA02405K.

[35] H. Yang, Q. Lin, C. Zhang, X. Yu, Z. Cheng, G. Li, Q. Hu, X. Ren, Q. Zhang, J. Liu, Carbon dioxide electroreduction on single-atom nickel decorated carbon membranes with industry compatible current densities, Nat. Commun. 11 (2020) 593, https://doi.org/10.1038/s41467-020-14402-0.

[36] H. Li, H. Li, P. Wei, Y. Wang, Y. Zang, D. Gao, G. Wang, X. Bao, Tailoring acidic microenvironments for carbon-efficient CO_2 electrolysis over Ni-NC catalyst in a membrane electrode assembly electrolyzer, Energy Environ. Sci. 16 (2023) 1502–1510, https://doi.org/10.1039/D2EE03482D.

[37] N.B. Watkins, Z.J. Schiffer, Y. Lai, C.B. Musgrave, H.A. Atwater, W.A. Goddard, T. Agapie, J.C. Peters, J.M. Gregoire, Hydrodynamics change tafel slopes in electrochemical CO_2 reduction on copper, ACS Energy Lett. 8 (2023) 2185–2192, https://doi.org/10.1021/ACSENERGYLETT.3C00442.

[38] S. Fu, M. Li, S. Asperti, W. De Jong, R. Kortlever, Unravelling the effect of activators used in the synthesis of biomass-derived carbon electrocatalysts on the electrocatalytic performance for CO_2 reduction, ChemSusChem 16 (2023) e202202188, https://doi.org/10.1002/CSSC.202202188.

[39] H. Yang, L. Shang, Q. Zhang, R. Shi, G.I.N. Waterhouse, L. Gu, T. Zhang, A universal ligand mediated method for large scale synthesis of transition metal single atom catalysts, Nat. Commun. 2019 101 10 (2019) 4585, https://doi.org/10.1038/s41467-019-12510-0.

[40] B. Endrődi, A. Samu, E. Kecsenovity, T. Halmágyi, D. Sebők, C. Janáky, Operando cathode activation with alkali metal cations for high current density operation of water-fed zero-gap carbon dioxide electrolysers, Nat. Energy 2021 64. 6 (2021) 439–448, https://doi.org/10.1038/s41560-021-00813-w.

[41] P. Lobaccaro, M.R. Singh, E.L. Clark, Y. Kwon, A.T. Bell, J.W. Ager, Effects of temperature and gas–liquid mass transfer on the operation of small electrochemical cells for the quantitative evaluation of CO_2 reduction electrocatalysts, Phys. Chem. Chem. Phys. 18 (2016) 26777–26785, https://doi.org/10.1039/C6CP05287H.

[42] Z. Wei, H. Qiao, H. Yang, C. Zhang, X. Yan, Characterization of NiO nanoparticles by anodic arc plasma method, J. Alloy. Compd. 479 (2009) 855–858, https://doi.org/10.1016/j.jallcom.2009.01.064.

[43] K. Artyushkova, B. Kiefer, B. Halevi, A. Knop-Gericke, R. Schlogl, P. Atanassov, Density functional theory calculations of XPS binding energy shift for nitrogen-containing graphene-like structures, Chem. Commun. 49 (2013) 2539–2541, https://doi.org/10.1039/C3CC40324F.

[44] D. Xi, J. Li, J. Low, K. Mao, R. Long, J. Li, Z. Dai, T. Shao, Y. Zhong, Y. Li, Z. Li, X. J. Loh, L. Song, E. Ye, Y. Xiong, Limiting the uncoordinated N Species in M–N_x single-atom catalysts toward electrocatalytic CO_2 reduction in broad voltage range, Adv. Mater. (2021) 2104090, https://doi.org/10.1002/ADMA.202104090.

[45] H.Bin Yang, S.F. Hung, S. Liu, K. Yuan, S. Miao, L. Zhang, X. Huang, H.Y. Wang, W. Cai, R. Chen, J. Gao, X. Yang, W. Chen, Y. Huang, H.M. Chen, C.M. Li, T. Zhang, B. Liu, Atomically dispersed Ni(i) as the active site for electrochemical CO_2 reduction, Nat. Energy 2018 32. 3 (2018) 140–147, https://doi.org/10.1038/s41560-017-0078-8.

[46] Z. Li, D. He, X. Yan, S. Dai, S. Younan, Z. Ke, X. Pan, X. Xiao, H. Wu, J. Gu, Size-dependent nickel-based electrocatalysts for selective CO_2 reduction, Angew. Chem. Int. Ed. 132 (2020) 18731–18736, https://doi.org/10.1002/anie.202000318.

[47] X. Rong, H. Wang, X. Lu, R. Si, T. Lu, Controlled synthesis of a vacancy-defect single-atom catalyst for boosting CO_2 electroreduction, Angew. Chem. Int. Ed. 132 (2020) 1977–1981, https://doi.org/10.1002/anie.201912458.

[48] S. Ma, P. Su, W. Huang, S.P. Jiang, S. Bai, J. Liu, Atomic Ni species anchored N-doped carbon hollow spheres as nanoreactors for efficient electrochemical CO_2 reduction, ChemCatChem 11 (2019) 6092–6098, https://doi.org/10.1002/CCTC.201901643.

[49] S. Fu, M. Li, W. de Jong, R. Kortlever, Tuning the properties of N-doped biochar for selective CO_2 electroreduction to CO, ACS Catal. 13 (2023) 10309–10323, https://doi.org/10.1021/ACSCATAL.3C01773.

[50] R. Boppella, M. Austeria, Y. Kim, E. Kim, I. Song, Y. Eom, D.Praveen Kumar, M. Balamurugan, E. Sim, H. Kim, T.K. Kim, Pyrrolic N-stabilized monovalent Ni single-atom electrocatalyst for efficient CO_2 reduction: identifying the role of pyrrolic–N and synergistic electrocatalysis, Adv. Funct. Mater. 32 (2022) 2202351, https://doi.org/10.1002/ADFM.202202351.

[51] H. Li, N. Xiao, M. Hao, X. Song, Y. Wang, Y. Ji, C. Liu, C. Li, Z. Guo, F. Zhang, J. Qiu, Efficient CO_2 electroreduction over pyridinic-N active sites highly exposed on wrinkled porous carbon nanosheets, Chem. Eng. J. 351 (2018) 613–621, https://doi.org/10.1016/J.CEJ.2018.06.077.

[52] W. Kou, Y. Zhang, J. Dong, C. Mu, L. Xu, Nickel-nitrogen-doped three-dimensional ordered macro-/mesoporous carbon as an efficient electrocatalyst for CO_2 Reduction to CO, ACS Appl. Energy Mater. 3 (2020) 1875–1882, https://doi.org/10.1021/ACSAEM.9B02324.

[53] W. Liu, S. Wei, P. Bai, C. Yang, L. Xu, Robust coal matrix intensifies electron/substrate interaction of nickel-nitrogen (Ni-N) active sites for efficient CO_2 electroreduction at industrial current density, Appl. Catal. B Environ. 299 (2021) 120661, https://doi.org/10.1016/J.APCATB.2021.120661.

[54] D. Hursán, A.A. Samu, L. Janovák, K. Artyushkova, T. Asset, P. Atanassov, C. Janáky, Morphological attributes govern carbon dioxide reduction on N-doped carbon electrodes, Joule 3 (2019) 1719–1733, https://doi.org/10.1016/j.joule.2019.05.007.

[55] C. Lim, W.H. Lee, J.H. Won, Y. Ko, S. Kim, B.K. Min, K. Lee, W.S. Jung, H. Oh, Enhancement of catalytic activity and selectivity for the gaseous electroreduction of CO_2 to CO: guidelines for the selection of carbon supports, Adv. Sustain. Syst. 5 (2021) 2100216, https://doi.org/10.1002/adsu.202100216.

[56] B.-Y. Cao, M. Chen, Z.-Y. Guo, Effect of surface roughness on gas flow in microchannels by molecular dynamics simulation, Int. J. Eng. Sci. 44 (2006) 927–937, https://doi.org/10.1016/j.ijengsci.2006.06.005.

[57] M.S. Faber, R. Dziedzic, M.A. Lukowski, N.S. Kaiser, Q. Ding, S. Jin, High-performance electrocatalysis using metallic cobalt pyrite (CoS_2) micro-and nanostructures, J. Am. Chem. Soc. 136 (2014) 10053–10061, https://doi.org/10.1021/ja504099w.

[58] X. Ma, J. Du, H. Sun, F. Ye, X. Wang, P. Xu, C. Hu, L. Zhang, D. Liu, Boron, nitrogen co-doped carbon with abundant mesopores for efficient CO_2 electroreduction, Appl. Catal. B Environ. 298 (2021) 120543, https://doi.org/10.1016/J.APCATB.2021.120543.

[59] M.-H. Sun, S.-Z. Huang, L.-H. Chen, Y. Li, X.-Y. Yang, Z.-Y. Yuan, B.-L. Su, Applications of hierarchically structured porous materials from energy storage and conversion, catalysis, photocatalysis, adsorption, separation, and sensing to biomedicine, Chem. Soc. Rev. 45 (2016) 3479–3563, https://doi.org/10.1039/C6CS00135A.

[60] L. Estevez, D. Barpaga, J. Zheng, S. Sabale, R.L. Patel, J.G. Zhang, B.P. McGrail, R. K. Motkuri, Hierarchically porous carbon materials for CO_2 capture: the role of pore structure, Ind. Eng. Chem. Res. 57 (2018) 1262–1268, https://doi.org/10.1021/acs.iecr.7b03879.

[61] W. Liu, J. Qi, P. Bai, W. Zhang, L. Xu, Utilizing spatial confinement effect of N atoms in micropores of coal-based metal-free material for efficiently electrochemical reduction of carbon dioxide, Appl. Catal. B Environ. 272 (2020) 118974, https://doi.org/10.1016/J.APCATB.2020.118974.

[62] Q. Wu, X. Yan, Y. Jia, X. Yao, Defective carbon-based materials: controllable synthesis and electrochemical applications, EnergyChem 3 (2021) 100059, https://doi.org/10.1016/J.ENCHEM.2021.100059.

[63] Q. Wu, J. Gao, J. Feng, Q. Liu, Y. Zhou, S. Zhang, M. Nie, Y. Liu, J. Zhao, F. Liu, J. Zhong, Z. Kang, A CO_2 adsorption dominated carbon defect-based electrocatalyst for efficient carbon dioxide reduction, J. Mater. Chem. A. 8 (2020) 1205–1211, https://doi.org/10.1039/C9TA11473D.

[64] W. Wang, L. Shang, G. Chang, C. Yan, R. Shi, Y. Zhao, G.I.N. Waterhouse, D. Yang, T. Zhang, Intrinsic carbon-defect-driven electrocatalytic reduction of carbon dioxide, Adv. Mater. 31 (2019) 1808276, https://doi.org/10.1002/adma.201808276.

[65] Y. Dong, Q. Zhang, Z. Tian, B. Li, W. Yan, S. Wang, K. Jiang, J. Su, C.W. Oloman, E. L. Gyenge, R. Ge, Z. Lu, X. Ji, L. Chen, Ammonia thermal treatment toward topological defects in porous carbon for enhanced carbon dioxide electroreduction, Adv. Mater. 32 (2020) 2001300, https://doi.org/10.1002/ADMA.202001300.

[66] D. Li, Y. Jia, G. Chang, J. Chen, H. Liu, J. Wang, Y. Hu, Y. Xia, D. Yang, X. Yao, A defect-driven metal-free electrocatalyst for oxygen reduction in acidic electrolyte, Chem 4 (2018) 2345–2356, https://doi.org/10.1016/j.chempr.2018.07.005.

[67] R. Daiyan, X. Tan, R. Chen, W.H. Saputera, H.A. Tahini, E. Lovell, Y.H. Ng, S. C. Smith, L. Dai, X. Lu, R. Amal, Electroreduction of CO_2 to CO on a mesoporous carbon catalyst with progressively removed nitrogen moieties, ACS Energy Lett. 3 (2018) 2292–2298, https://doi.org/10.1021/ACSENERGYLETT.8B01409.

[68] L. Ling, L. Jiao, X. Liu, Y. Dong, W. Yang, H. Zhang, B. Ye, J. Chen, H. Jiang, Potassium-assisted fabrication of intrinsic defects in porous carbons for electrocatalytic CO_2 Reduction, Adv. Mater. 34 (2022) 2205933, https://doi.org/10.1002/adma.202205933.

[69] S. Gupta, S. Zhao, O. Ogoke, Y. Lin, H. Xu, G. Wu, Engineering favorable morphology and structure of Fe-N-C oxygen-reduction catalysts through tuning of nitrogen/carbon precursors, ChemSusChem 10 (2017) 774–785, https://doi.org/10.1002/cssc.201601397.

[70] L. Ning, S. Liao, H. Li, R. Tong, C. Dong, M. Zhang, W. Gu, X. Liu, Carbon-based materials with tunable morphology confined Ni (0) and Ni-N_x active sites: highly efficient selective hydrogenation catalysts, Carbon 154 (2019) 48–57, https://doi.org/10.1016/j.carbon.2019.07.099.

[71] J.F. Watts, J. Wolstenholme, An introduction to surface analysis by XPS and AES, John Wiley & Sons, 2019, https://doi.org/10.1002/0470867930.

[72] F. Bienen, M.C. Paulisch, T. Mager, J. Osiewacz, M. Nazari, M. Osenberg, B. Ellendorff, T. Turek, U. Nieken, I. Manke, Investigating the electrowetting of silver-based gas-diffusion electrodes during oxygen reduction reaction with electrochemical and optical methods, Electrochem. Sci. Adv. 3 (2023) e2100158, https://doi.org/10.1002/elsa.202100158.